Export Authority :
22CFR 125.4 (b) (13)

PREDICTION OF INVISCID SUPERSONIC/HYPERSONIC AIRCRAFT FLOWFIELDS

A. Verhoff† and D. Stookesberry‡
McDonnell Douglas Corporation
McDonnell Aircraft Company
St. Louis, Missouri

Abstract

A spatial marching method called SCRAM has been developed to numerically solve the Euler equations for supersonic and hypersonic flow. The equations are formulated in terms of Riemann-type variables using a local streamline coordinate system. Expressed in this way, the equations model wave propagation in a very physical manner with no high Mach number restrictions. High computational efficiency is achieved on a vector processor such as a CRAY or CONVEX. The procedure has been coupled with a versatile grid generation method which automatically sections complex cross-sectional grids into simpler domains on the basis of singular geometry points, such as sharp internal or external corners. SCRAM predictions have been validated by comparison with test data for several realistic aircraft configurations, including cases having non-zero sideslip. The comparisons include force and moment data and surface pressure data. A fully-iterative procedure has been implemented to start the SCRAM code for arbitrary blunt-nosed configurations and also to handle embedded subsonic regions. An efficient procedure for predicting the effect of control surface deflections has been incorporated and validated against test data. Real gas results for a cone are compared with the analytic solution.

Introduction

A method has been developed for accurate, efficient prediction of supersonic and hypersonic inviscid flowfields. It uses a spatial marching procedure to numerically approximate the solution of the QAZ1D form of the Euler equations presented in Reference 1. This formulation is unique in that the equations are written in terms of Riemann-type variables using a natural streamline coordinate system. Because of this, the equations model wave propagation in a very physical manner with no Mach number limitations. Equally important is the ease with which the associated numerical solution procedure can be coded and the high efficiency which can be achieved on a vector processor such as the CRAY XMP or CONVEX C1/C2.

Because the QAZ1D Euler formulation describes the physical process of wave propagation and has no inherent Mach number restrictions, it lends itself readily to supersonic and hypersonic flowfield analysis. A computer program called SCRAM (Streamline Coordinate Riemann Axial Marching) has been developed (References 2 and 3) based upon the QAZ1D formulation. For fully supersonic inviscid flow, 3D flowfield analysis can be reduced to a sequence of 2D problems by using a spatial marching solution procedure.

Many existing marching procedures use the longitudinal body axis as the primary direction of information propagation. This requires the velocity in the body axis direction to be supersonic. The QAZ1D formulation uses a local streamline-oriented coordinate system at each grid point in the flowfield to propagate information downstream in a much more physically accurate manner. As a result, flowfields about configurations having wings, tails, fins, etc., can be accurately predicted using relatively coarse computational grids. Supersonic flow is required, but the velocity in the marching direction is only required to be positive.

Results from the SCRAM code are presented for several aircraft configurations, including cases with a nonzero yaw angle. Predicted force and moment coefficients and surface pressures are compared with available test data. Included are flowfields having embedded subsonic regions which are handled by local application of a fully-iterative method. Predictions of control surface effectiveness are also presented. A real gas version of SCRAM has been developed for analysis at hypersonic Mach numbers. For validation purposes, comparisons of surface density and shock wave angle are made with analytic solutions for a circular cone.

Governing Equations

The fluid dynamic equations on which the SCRAM code is based are the three-dimensional Euler equations which describe inviscid flow. In terms of (characteristic-type) extended Riemann variables in natural streamline coordinates (s,n,m), these equations are (Reference 1)

$$\frac{\partial Q}{\partial t}+(q+a)\frac{\partial Q}{\partial s} = -\frac{\gamma-1}{2}a(S-\frac{2}{\gamma-1})[\frac{\partial}{\partial s}(q-\frac{2}{\gamma-1}a)] - \frac{\gamma-1}{2}qaS[\frac{\partial \theta}{\partial n}+\cos\theta\frac{\partial \phi}{\partial m}]$$

$$\frac{\partial R}{\partial t}+(q-a)\frac{\partial R}{\partial s} = +\frac{\gamma-1}{2}a(S-\frac{2}{\gamma-1})[\frac{\partial}{\partial s}(q+\frac{2}{\gamma-1}a)] + \frac{\gamma-1}{2}qaS[\frac{\partial \theta}{\partial n}+\cos\theta\frac{\partial \phi}{\partial m}]$$

$$\frac{\partial S}{\partial t}+q\frac{\partial S}{\partial s} = 0 \qquad (1)$$

† Principal Technical Specialist – Aerodynamics
‡ Senior Engineer – Aerodynamics

$$\frac{\partial \theta}{\partial t} + q\frac{\partial \theta}{\partial s} = -\frac{a^2}{\gamma q}\frac{\partial \ln p}{\partial n}$$

$$\frac{\partial \phi}{\partial t} + q\frac{\partial \phi}{\partial s} = -\frac{a^2}{\gamma q \cos\theta}\frac{\partial \ln p}{\partial m}$$

The extended Riemann variables are defined as

$$\begin{aligned} Q &= q + aS \\ R &= q - aS \end{aligned} \tag{2}$$

where q is the velocity magnitude and a is the speed of sound. Time is denoted by t. The modified entropy S is defined in terms of pressure p, density ρ, and the ratio of specific heats γ by the relation

$$S \equiv \frac{1}{\gamma(\gamma-1)}[2\gamma - \ln(\frac{p}{\rho^\gamma})] \tag{3}$$

The above relationships assume that the gas is perfect.

The flow angles θ and ϕ are defined as shown in Figure 1. Also shown is the natural streamline coordinate system (s,n,m) with respect to a fixed rectangular Cartesian system (x,y,z). The natural system is orthogonal in that 's' is measured in the direction of flow, 'n' lies in the plane defined by the y-axis and the s-coordinate direction, and 'm' is normal to the (s,n) plane. At each point in the computational grid, the system of equations is expressed in the streamline coordinate system local to that point.

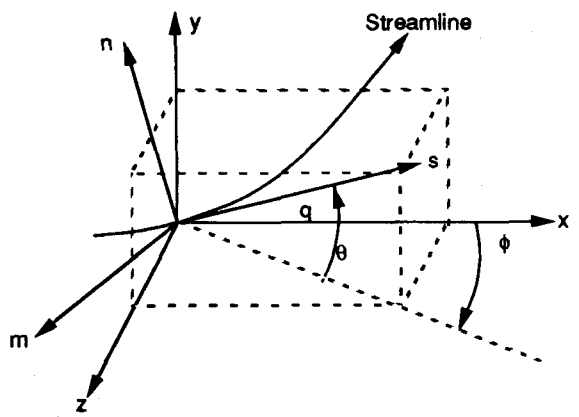

Fig. 1 Definition of Flow Angles and Streamline Coordinates

At hypersonic speeds, high temperature effects such as ionization, dissociation and recombination of the various gas species can strongly influence the flowfield. Under these conditions the perfect gas law must be replaced with a model which accounts for high temperature effects. In the SCRAM code an equilibrium air model is used based on the following three relationships

$$\begin{aligned} \beta &= fn(h,S) \\ \gamma_e &= fn(h,S) \\ z &= fn(h,S) \end{aligned} \tag{4}$$

where

$$\beta = \frac{h}{e}, \qquad \gamma_e = \frac{a^2\rho}{p}, \qquad z = \frac{p}{\rho \mathcal{R} T} \tag{5}$$

The variable $\mathcal{R}$ is the gas constant, T is temperature, h is enthalpy, and e is internal energy. Using this model, the Euler equations (1) become

$$\begin{aligned} \frac{\partial Q}{\partial t} + (q+a)\frac{\partial Q}{\partial s} &= a(S - \frac{2}{\beta-1})[\frac{\partial a}{\partial s} - \frac{\beta-1}{2}\frac{\partial q}{\partial s}] \\ &- \frac{\beta-1}{2}qaS[\frac{\partial \theta}{\partial n} + \cos\theta\frac{\partial \phi}{\partial m}] + \frac{2}{\beta-1}a(1-\frac{\beta}{\gamma_e})\frac{\partial a}{\partial s} \\ &+ a^2(1 - \frac{\gamma_\infty}{\gamma_e}\frac{1}{z})\frac{\partial S}{\partial s} + \frac{1}{2}qaS[\frac{1}{\beta-1}\frac{\partial \beta}{\partial s} + \frac{1}{\gamma_e}\frac{\partial \gamma_e}{\partial s}] \\ &+ \frac{1}{\beta-1}\frac{1}{\gamma_e}a^2[\frac{1}{\beta-1}\frac{\partial \beta}{\partial s} + \frac{\beta}{\gamma_e}\frac{\partial \gamma_e}{\partial s}] \end{aligned}$$

$$\begin{aligned} \frac{\partial R}{\partial t} + (q-a)\frac{\partial Q}{\partial s} &= a(S - \frac{2}{\beta-1})[\frac{\partial a}{\partial s} + \frac{\beta-1}{2}\frac{\partial q}{\partial s}] \\ &+ \frac{\beta-1}{2}qaS[\frac{\partial \theta}{\partial n} + \cos\theta\frac{\partial \phi}{\partial m}] + \frac{2}{\beta-1}a(1-\frac{\beta}{\gamma_e})\frac{\partial a}{\partial s} \\ &+ a^2(1 - \frac{\gamma_\infty}{\gamma_e}\frac{1}{z})\frac{\partial S}{\partial s} - \frac{1}{2}qaS[\frac{1}{\beta-1}\frac{\partial \beta}{\partial s} + \frac{1}{\gamma_e}\frac{\partial \gamma_e}{\partial s}] \\ &+ \frac{1}{\beta-1}\frac{1}{\gamma_e}a^2[\frac{1}{\beta-1}\frac{\partial \beta}{\partial s} + \frac{\beta}{\gamma_e}\frac{\partial \gamma_e}{\partial s}] \end{aligned}$$

$$\frac{\partial S}{\partial t} + q\frac{\partial S}{\partial s} = 0 \tag{6}$$

$$\frac{\partial \theta}{\partial t} + q\frac{\partial \theta}{\partial s} = -\frac{a^2}{\gamma_e q}\frac{\partial \ln p}{\partial n}$$

$$\frac{\partial \phi}{\partial t} + q\frac{\partial \phi}{\partial s} = -\frac{a^2}{\gamma_e q \cos\theta}\frac{\partial \ln p}{\partial m}$$

where

$$\begin{aligned} \frac{\partial \ln p}{\partial n} &= \frac{2}{\beta-1}\frac{\beta}{a}\frac{\partial a}{\partial n} + \frac{\gamma_\infty}{z}\frac{\partial S}{\partial n} \\ &- \frac{1}{\beta-1}[\frac{1}{\beta-1}\frac{\partial \beta}{\partial n} + \frac{\beta}{\gamma_e}\frac{\partial \gamma_e}{\partial n}] \\ \frac{\partial \ln p}{\partial m} &= \frac{2}{\beta-1}\frac{\beta}{a}\frac{\partial a}{\partial m} + \frac{\gamma_\infty}{z}\frac{\partial S}{\partial m} \\ &- \frac{1}{\beta-1}[\frac{1}{\beta-1}\frac{\partial \beta}{\partial m} + \frac{\beta}{\gamma_e}\frac{\partial \gamma_e}{\partial m}] \end{aligned} \tag{7}$$

The quantity γ_∞ is the ratio of specific heats for a perfect gas. To provide consistency with the perfect gas system (1), the modified entropy S is defined by the relation

$$S = \frac{-s}{\gamma_\infty \mathcal{R}} \tag{8}$$

where s is the specific entropy. At low temperatures where the perfect gas assumption is valid, equation set (6) is equivalent to equation set (1).

Solution Methodology

The various elements of the solution methodology used in the SCRAM code are described below.

Numerical Solution Algorithm

At each successive cross-sectional plane, the QAZ1D Euler equations (1) or (6) are relaxed to steady-state using explicit time integration. Streamwise spatial derivatives are approximated by three-point one-sided (upstream) finite differences to properly model the wave propagation. Derivatives normal to the streamline direction are decomposed and approximated with three-point one-sided differences determined by the local direction of wave propagation. The characteristic analysis for the decomposition can be outlined simply for the case of isentropic 2D flow. In matrix notation the QAZ1D equations under these assumptions have the form

$$\{F\}_t + [A]\{F\}_s + [B]\{F\}_n = 0 \qquad (9)$$

where $\{F\}$ is the column vector of dependent variables and $[A]$ is the diagonal matrix of characteristic velocities. Subscripts s and n refer to derivatives along and normal to the local streamline direction. In order to distinguish directions of propagation normal to the local streamline direction, the B matrix is transformed according to

$$[B] = [X][\lambda][X]^{-1} \qquad (10)$$

This provides the rule for splitting the B matrix into

$$[B] = [B^+] + [B^-] \qquad (11)$$

where $[B^+]$ and $[B^-]$ each have a unique direction of propagation based on the eigenvalue sign. Splitting the B matrix allows numerical differencing normal to the streamline direction which is consistent with the physical direction of wave propagation. It acts to inhibit any odd-even decoupling of the solution (saw-tooth pattern) sometimes observed with central-difference approximations. Although it produces a dissipative truncation error similar to "artificial viscosity", it is not artificial because the coefficients of the dissipative terms are not arbitrary. A more detailed description of the characteristic analysis may be found in Reference 4.

To accelerate the convergence to steady state in each cross-plane, local maximum time steps are used along with a checkerboard (odd-even) scheme. The resulting formulation is almost completely vectorizable on CRAY XMP and CONVEX computers. Nonphysical input parameters are not used in the solution algorithm.

Grid Generation

Accurate calculation of flowfield quantities is highly dependent on the quality of the computational grid regardless of the flowfield solution procedure. The grid must accurately resolve the body shape in addition to being nearly orthogonal and smoothly varying, particularly near the body surface.

The surface-conforming grid generation method that was developed for the SCRAM code evolved from the method presented in Reference 5. The grid is generated by solving an elliptic system of partial differential equations. Forcing functions of the type described in Reference 6 allow strong localized control of node spacing and grid orthogonality on and near grid boundaries. Moreover, this grid control near boundaries allows multiple grid blocks to be generated independently and matched smoothly at their common boundaries. This feature is particularly useful for the geometries characteristic of hypersonic vehicle concepts.

For the H-O topology used within the SCRAM code marching procedure, the entire 3D grid is constructed by successive generation of 2D grids at each longitudinal station of interest. For most cases symmetry boundary conditions are imposed at the center-plane so that only one-half of the 2D cross-section (half-plane) is used. For unsymmetrical cross-sections or cases with sideslip, the entire cross-section (full-plane) is used. The 2D grid code automatically sections a complex domain into a number of simpler domains on the basis of singular geometry points such as sharp internal or external corners. A high quality grid is then generated for each of the simpler sections. The sections are matched smoothly at their common boundaries due to the nearly complete control of the grid in the vicinity of boundaries. The procedure is automatic, not user interactive.

Starting Solution

A supersonic starting-plane solution is required to initiate the downstream marching procedure. For sharp-nosed configurations it is assumed that a small region about the nose may be modeled by conical flow. The local conical flowfield solution is obtained by guessing a starting plane solution and shock geometry. An iterative "step-back" procedure is then used. A downstream step is taken assuming the geometry is conical, and the solution is converged in this plane. This solution is transferred back to the original starting plane location under the assumption of conical flow. This process is repeated until the solution and shock geometry being transferred back to the starting plane are unchanged from the previous cycle. This starting plane solution is then used to continue the solution downstream for the actual geometry. Procedures for other shapes (*e.g.*, blunt nose) are described in detail below.

Surface Boundary Conditions

During the transient solution process in each cross-plane, a local velocity vector tangent to a solid boundary surface will respond to the local pressure gradient on the surface. Since the streamlines are constrained to the body surface, the velocity vector can only rotate in the local tangency plane. Because of this, the flow angles θ and ϕ are algebraically related. With the QAZ1D formulation,

the surface boundary calculation is reduced locally to a two-dimensional problem on the tangent plane at a given surface grid point. The pressure gradient normal to the streamline in the tangent plane dictates the deflection required of the local velocity vector. Once the new velocity vector orientation is known, the corresponding changes to θ and ϕ are easily determined.

Shock Wave Treatment

Bow shock waves can be fitted within the SCRAM formulation using the Rankine-Hugoniot relations to obtain flow conditions behind the shock. As the solution is converged in each cross plane, the grid outer boundary is adjusted along radial grid lines to conform to the shock shape. The grid is then rescaled within SCRAM to the new outer boundary shape. Secondary shock waves are captured isentropically. These waves tend to be weaker than the bow wave and can usually be approximated as isentropic. An option also exists to capture the bow shock isentropically. An evaluation of isentropic shock capturing error using this option is given in Reference 2. Within the typical supersonic operating envelope of fighter aircraft, a bow shock wave captured isentropically results in local pressure errors of well below 1 percent. Although more calculations are required for bow shock fitting, the overall number of grid points is reduced because the grid need not extend beyond the shock wave. Because the shock fitting calculations vectorize, there is only a slight increase in computational cost when the shock fitting option is used.

Capabilities and Applications

Numerical solutions have been computed for many different geometries in order to demonstrate the ability of SCRAM to predict flowfields about realistic aircraft configurations. Comparisons with test data have been made whenever possible. Representative examples are presented below.

Cambered Shapes

Flowfield predictions were made for the cambered fighter forebody of Reference 7. This geometry has a highly cambered strake and a sharp wing leading edge. The surface grid is shown in Figure 2. The grid is composed of three sections with half-plane dimensions 61x19x6, 85x35x11, and 85x41x21, respectively. Longitudinal patching allowed a smooth transfer of flowfield data between grids while maintaining adequate grid definition of the surface. At the bow shock the shock fitting boundary condition was used. Force and moment predictions are shown in Figure 3 for a free stream Mach number of 1.8. An estimate of the skin friction drag has been added to the SCRAM results. The agreement with test data is good, especially for inviscid supersonic drag. Predicted spanwise surface pressure distributions compared with test data at three axial stations are shown in Figure 4 along with the corresponding off-body pressure contours. The SCRAM predictions agree well with test data although the inviscid cross-flow shock location is slightly in error at this relatively large angle of attack. Predicted centerline pressures are also compared with test data.

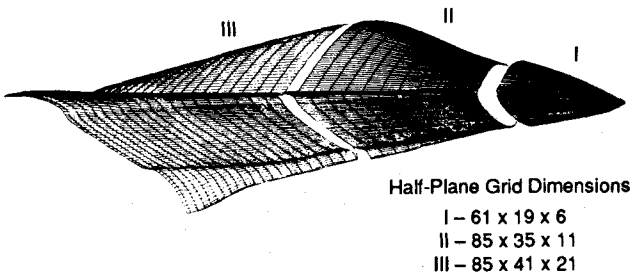

Fig. 2 Surface Grid for Cambered Fighter Forebody

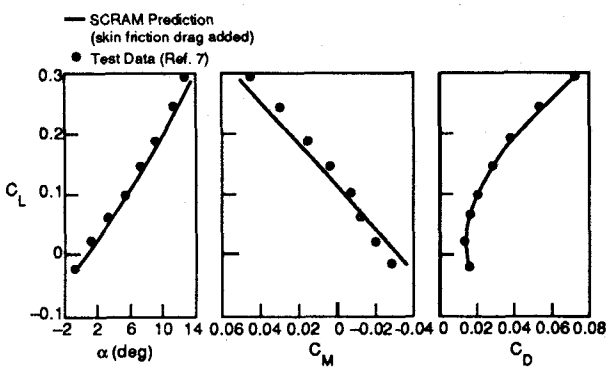

Fig. 3 Force and Moment Predictions for Cambered Fighter Forebody
$M_\infty = 1.8$

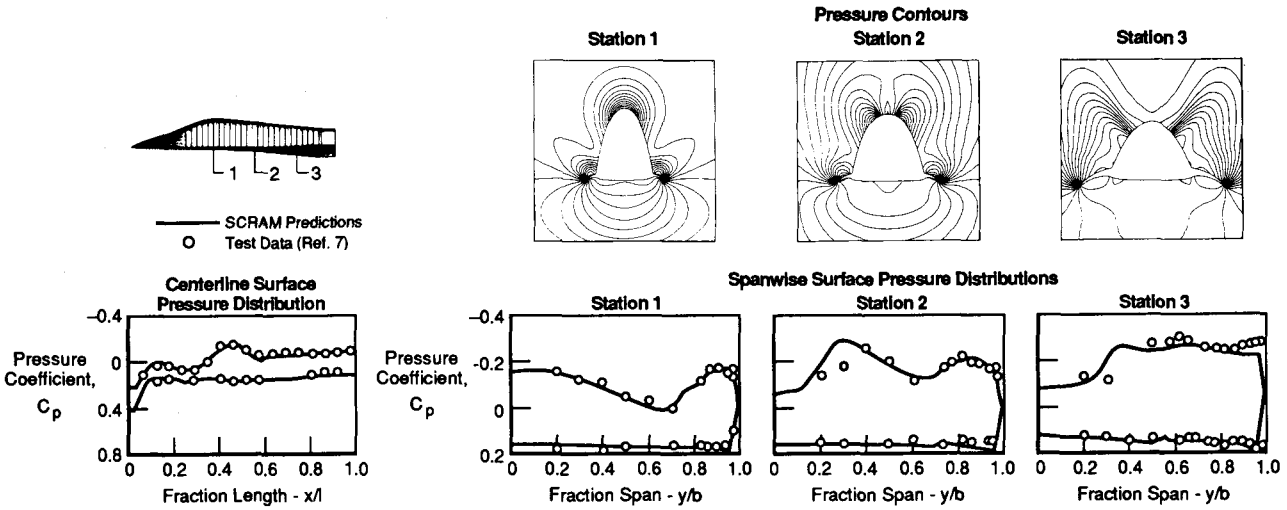

Fig. 4 Pressure Predictions for Cambered Fighter Forebody
$M_\infty = 1.8 \quad \alpha = 13°$

Sideslip Capability

Most SCRAM computations can be carried out using a half-plane grid with symmetry boundary conditions to reduce computer time. Because of its low CPU and computer memory requirements, SCRAM can efficiently run full-plane grids for non-symmetric vehicles or sideslip conditions. The hypersonic research vehicle of Reference 8 provides a good wind tunnel data base for validating the sideslip capability of SCRAM. Figure 5 shows the surface grid which had full-plane dimensions 121x15x25. Flowfield predictions were made at a free stream Mach number of 3.46 and sideslip angle β between -4.0 to 11.0 degrees. The solutions were obtained using the shock fitting option in SCRAM. Lateral force and moment predictions are shown in Figure 6 for 0.0 and 4.0 degrees angle of attack. The comparison with test data is very good for both angles of attack throughout the range of sideslip angle. The SCRAM side force prediction begins to depart slightly from test data at the largest sideslip angle. This is probably due to the onset of separation on the tail surface. Computer run times for the different cases were between 12 and 15 minutes on a CRAY XMP-18.

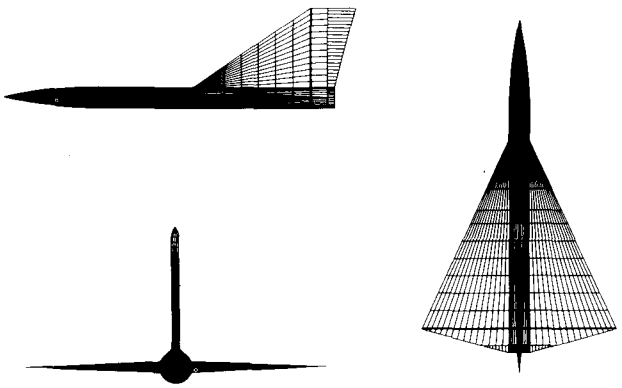

Fig. 5 Surface Grid for Hypersonic Research Vehicle

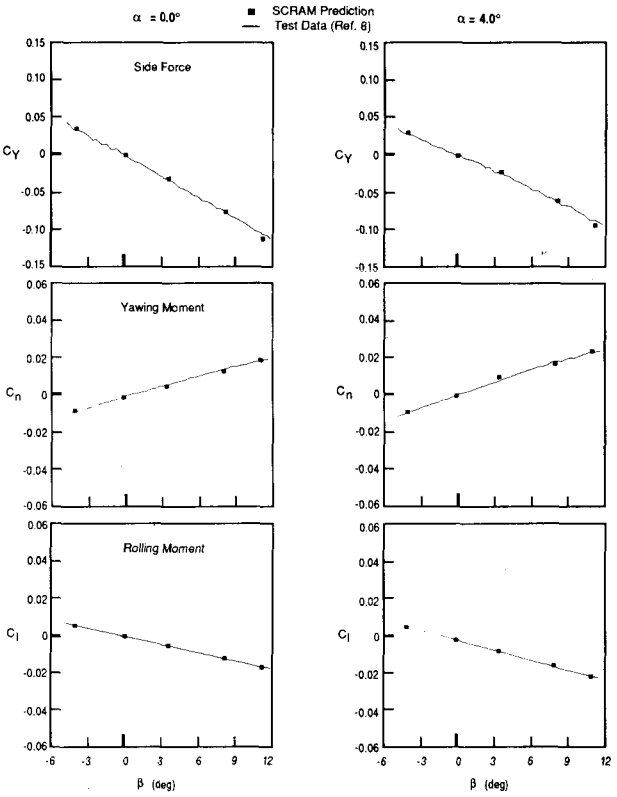

Fig. 6 Lateral Force and Moment Predictions for Hypersonic Research Vehicle
$M_\infty = 3.46$

Arbitrary Nose Shapes

An option is included in SCRAM to generate a starting plane solution for wedge-type forebodies. The approach assumes that the forebody leading edge region is a two-dimensional wedge and the bow shock angle and flow quantities on the upper and lower leading edge surfaces are obtained using oblique shock and expansion wave theory. The downstream marching procedure is then initiated from this "slit" of double valued initial conditions. Force and moment predictions for a wedge-type forebody are presented in Figure 7. A half-plane grid of 49x15x9 was used. The SCRAM predictions compare well with the test data of Reference 9. An adjustment for skin friction drag was not made to the SCRAM predictions.

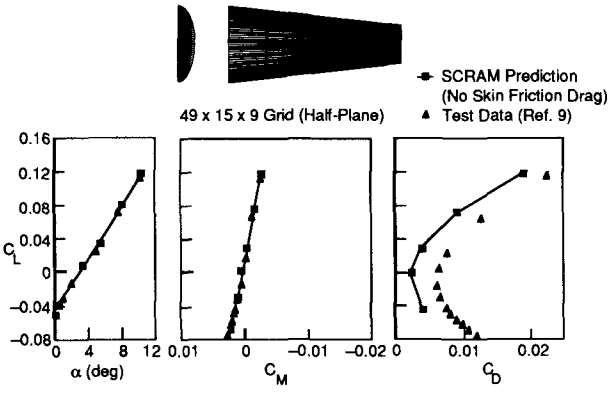

Fig. 7 Force and Moment Predictions for Wedge Forebody
$M_\infty = 5.0$

For blunt-nosed configurations a subsonic flow region exists between the bow shock and the body. A starting plane solution for SCRAM must be provided at a location where the flow has become fully supersonic. An option in SCRAM computes a three-dimensional blunt nose flow solution with a fully iterative procedure. The H-O grid near the front of the configuration is converted to a C-O grid with a singular line emanating from the nose. Solution of the Euler equations is carried out simultaneously at a number of cross-sectional planes encompassing the subsonic region. This procedure allows information from all directions to be utilized in the calculation. The space-marching procedure is then used downstream from where the flow becomes supersonic. By using the QAZ1D formulation and the shock fitting option, consistency is provided between the nose tip solution and the marching solution.

The starting procedure has been validated for various blunt nose geometries. Figure 8 shows the predicted surface pressure distribution for a blunt cone/cylinder geometry at a free stream Mach number of 4.95. The predictions agree well with flight test data (Reference 10) up to the sharp expansion corner. A small region of flow separation exists downstream of the corner which an inviscid code such as SCRAM will not predict. The predicted shock wave shape for a cylinder with a spherical nose cap at a free stream Mach number of 3.0 is shown in Figure 9. The comparison with test data (Reference 11) is very good. For both of these computed results, a smooth transition is obtained between the fully-iterative starting solution and the marching solution.

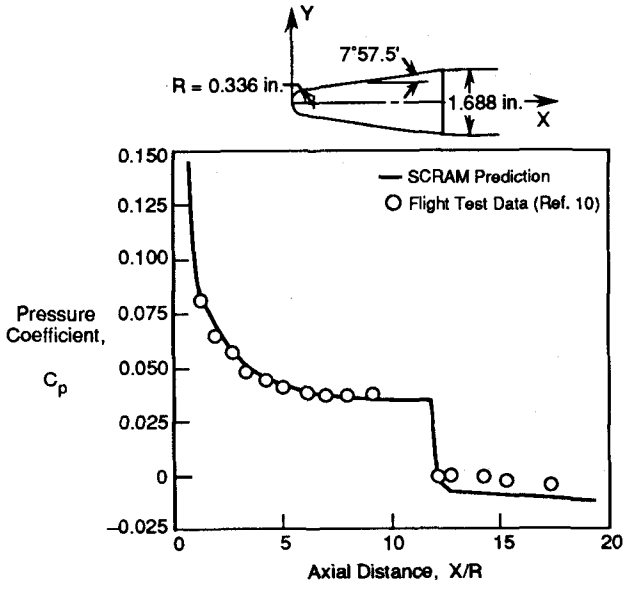

Fig. 8 Surface Pressure Distribution for Blunt Cone/Cylinder
$M_\infty = 4.95 \quad \alpha = 0°$

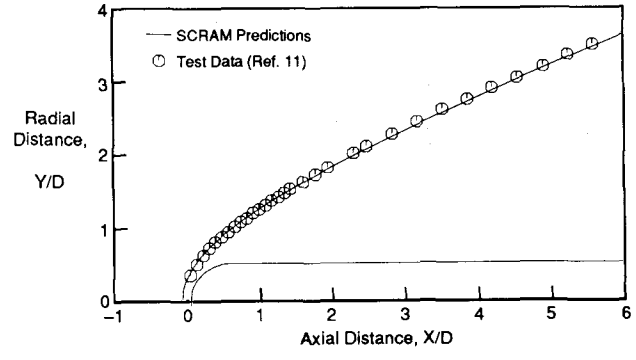

Fig. 9 Shock Location for Hemisphere/Cylinder
$M_\infty = 3.0 \quad \alpha = 0°$

As a further demonstration of SCRAM capability, the flowfield about the lifting body geometry of Reference 12 was computed at a free stream Mach number of 3.0. Figure 10 shows the surface portion of the computational grid which had half-plane dimensions 61x13x49. Also shown are pressure contours on the surface and centerplane and the bow shock location. The starting solution extends onto the flat upper surface in order to ensure supersonic flow for the marching procedure. The transition

between the starting solution and the marching solution is smooth.

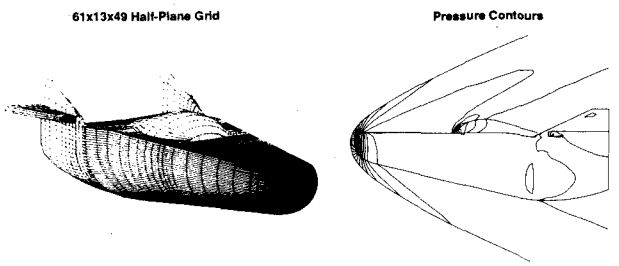

Fig. 10 Pressure Contours for Lifting Body Geometry
$M_\infty = 3.0 \quad \alpha = 0.5°$

Subsonic Regions

Occasionally at a canopy-fuselage or wing-fuselage juncture a small region of subsonic flow may occur which will cause a breakdown in the marching (supersonic) solver. An example is the lifting body geometry described previously (see Figure 10). When a subsonic point is detected, SCRAM will write a restart file from the last supersonic station and stop. The solution procedure can be restarted by using a fully iterative routine (similar to the blunt-nose solver) over a specified number of stations. When a longitudinal station is reached where the flowfield again becomes fully supersonic, SCRAM will switch back to the marching solver to save execution time and computer memory. For the case of the lifting body, the blunt-nose routine was used to start the solution. The marching solver was then used up to the canopy. At the front of the canopy the subsonic routine was used and then at the top of the canopy SCRAM switched back to the marching solver for the rest of the body.

Inlet/Nozzle Capability

For complete configurations SCRAM can model engine inlets and nozzles. At the inlet face, the mass flow is removed from the flowfield assuming no spillage. This mass flow can be added back at a nozzle face to simulate an engine. At the nozzle exit face, arbitrary flow conditions can be imposed. A demonstration of the inlet/nozzle capability can be found in Reference 3.

Flow-Through Boundary

For vehicle geometries that have aft-swept trailing edges or an over-hanging empennage, isolated solid surfaces appear in the cross-plane flowfield. A wake surface is used to connect the solid surfaces and a flow-through boundary condition is applied. To demonstrate the procedure, force and moment predictions are presented in Figure 11 for an arrow wing/body configuration at a free stream Mach number of 3.0. The predictions compare well with the test data of Reference 13. An estimate for skin friction drag was not added to the SCRAM predictions. Figure 12 shows a cross-sectional view of the flow-through boundary. Pressure contours are also shown along with the shock-fitted grid. Note that the contour lines cross the flow-through boundary smoothly.

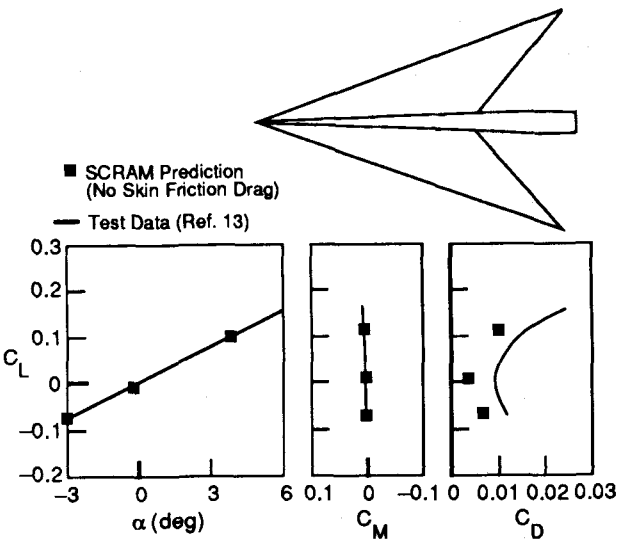

Fig. 11 Force and Moment Predictions
for Arrow Wing/Body
$M_\infty = 3.0$

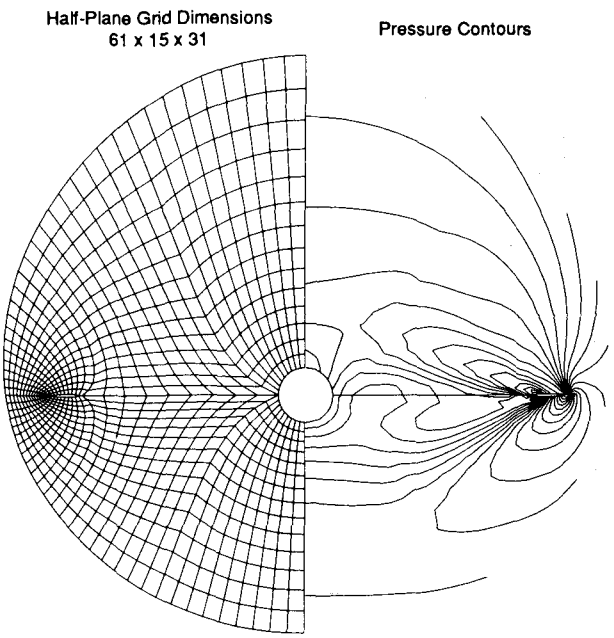

Fig. 12 Arrow Wing Flow-Through
Boundary Illustration
$M_\infty = 3.0 \quad \alpha = 4°$

Zonal Grid Capability

A single surface-conforming grid is sometimes not adequate to define the surface curvature or associated off-body field of complex configurations. Additional zones or subgrids may be introduced within SCRAM to define complex regions (*e.g.*, between vertical tails, around missiles,

etc.). Boundary conditions at the zone interfaces are modified to transfer flow information between the main grid and the subgrids.

Figure 13 shows an example of how a zonal grid can greatly improve grid resolution quality. Using a single grid causes grid lines to become highly skewed with inadequate grid density on the surface. Crossed grid lines would cause failure of the flow solver. When a zonal grid is used, there is adequate grid definition between the tails and between the wing and store. A demonstration of zonal grid flow solution capability is shown in Figure 14. Even with point mismatch, the pressure contours are smooth along the grid interfaces.

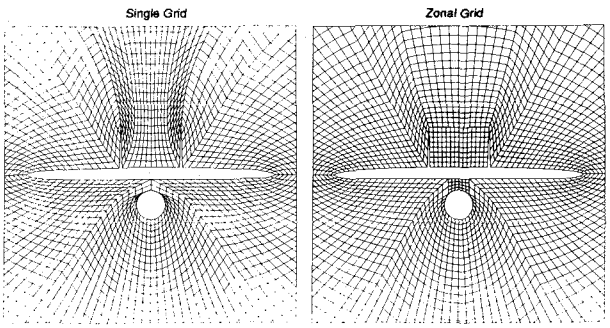

Fig. 13 Zonal Grid Demonstration

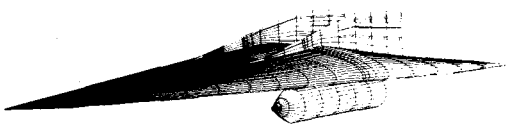

Pressure Contours

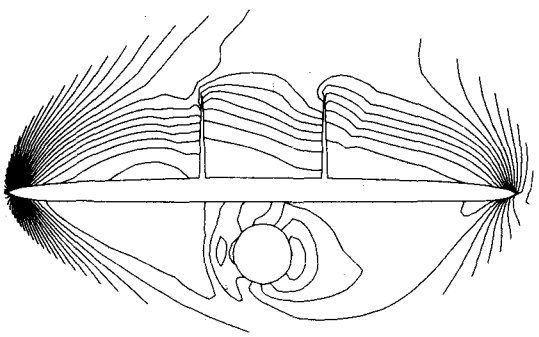

Cross-Flow Velocity Vectors

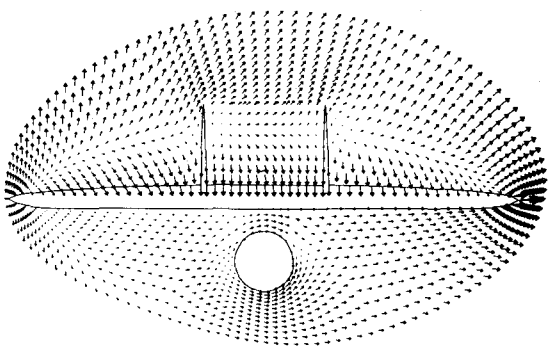

Fig. 14 Zonal Grid Flow Solution for a Generic Configuration
$M_\infty = 7.4 \quad \alpha = 2° \quad \beta = 3°$

Control Surface Deflections

As part of the aircraft design process, SCRAM may be used to evaluate the effectiveness of various movable control surfaces. The control surface can be any "trailing-edge" type surface (*e.g.*, aileron, elevon, rudder). To account for surface deflection, SCRAM adjusts the local flow angle on the vehicle surface similar to a surface blowing or suction boundary condition. The grid is not altered from the zero deflection case and cannot account for the gap between the control surface and the adjacent geometry. Grid points on a control surface are flagged and the boundary condition is adjusted based on grid point location, input hinge line, and input deflection angle. The control surface can be full or partial span and the hinge line may be swept. A series of deflection angles can be efficiently run by restarting the solution upstream of the control surface and changing the deflection angle in the input file.

Elevon control power predictions were made for the Supersonic Persistent Fighter (SSPF) model of Reference 14. Calculations were made using a faired inlet forebody geometry. Figure 15 shows the surface grid and the actual model configuration. Predicted elevon control power increments are compared with test data in Figure 16 for a free stream Mach number of 2.0. Control surfaces were deflected upward 5 and 10 degrees. The agreement with test data is good. A zero-deflection case required approximately 12 minutes execution time on a CRAY XMP-18 computer. Subsequent deflected surface cases required about 2 minutes each. The zonal grid capability described above was used to define the area between the vertical tails. Including the vertical tails in the analysis improved the moment prediction by introducing the nonlinearity in the moment curve at the high deflection angle.

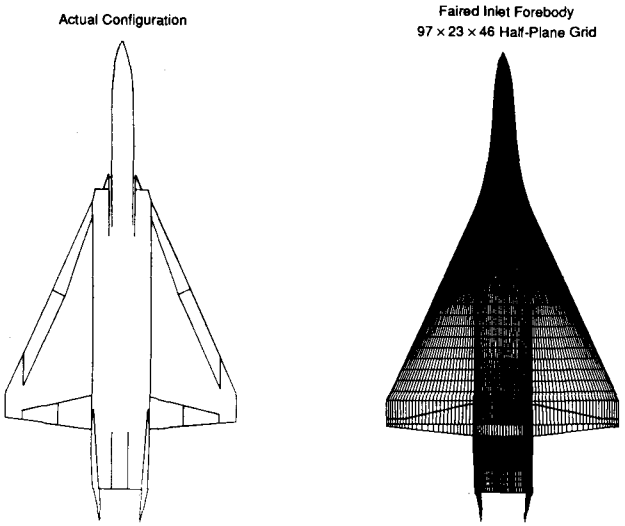

Fig. 15 Surface Grid for Supersonic Persistent Fighter (SSPF) Model

Real Gas Effects

At hypersonic speeds the perfect gas law must be replaced with a real gas model as outlined earlier. Initially a version of the NASA RGAS program (Reference 15) was used to compute the gas properties required in equations (6). Because the RGAS program requires a large amount of computer time, new curve fits (called TMGAS) of the RGAS data were generated. The TMGAS curve fits are similar in construction to the TGAS curve fits of Reference 16 except that enthalpy and entropy are the independent variables. The execution time of SCRAM was improved by a factor of two when TMGAS was used instead of RGAS.

Surface densities predicted by the real gas SCRAM code (called RSCRAM) are compared in Figure 17 with the analytical calculations of Reference 17 for a circular cone in equilibrium air. At lower Mach numbers ($M_\infty <$ 10) predictions agree well with perfect gas theory. At high Mach numbers, predictions agree well with the analytical theory of hypersonic conical flow. Solutions obtained using the TMGAS model are nearly identical to those obtained using the RGAS model.

Accurate prediction of bow shock-wave shape is especially important for hypersonic vehicles where the engine inlet often lies just inside the bow wave. Shock position can be strongly influenced by real gas effects. Shock-wave angles predicted by RSCRAM for a cone are presented in Figure 18. The predictions show excellent agreement with the analytical results of Reference 17. Computer run times for the real gas version of SCRAM are typically 40 to 50 percent more than for the perfect gas version.

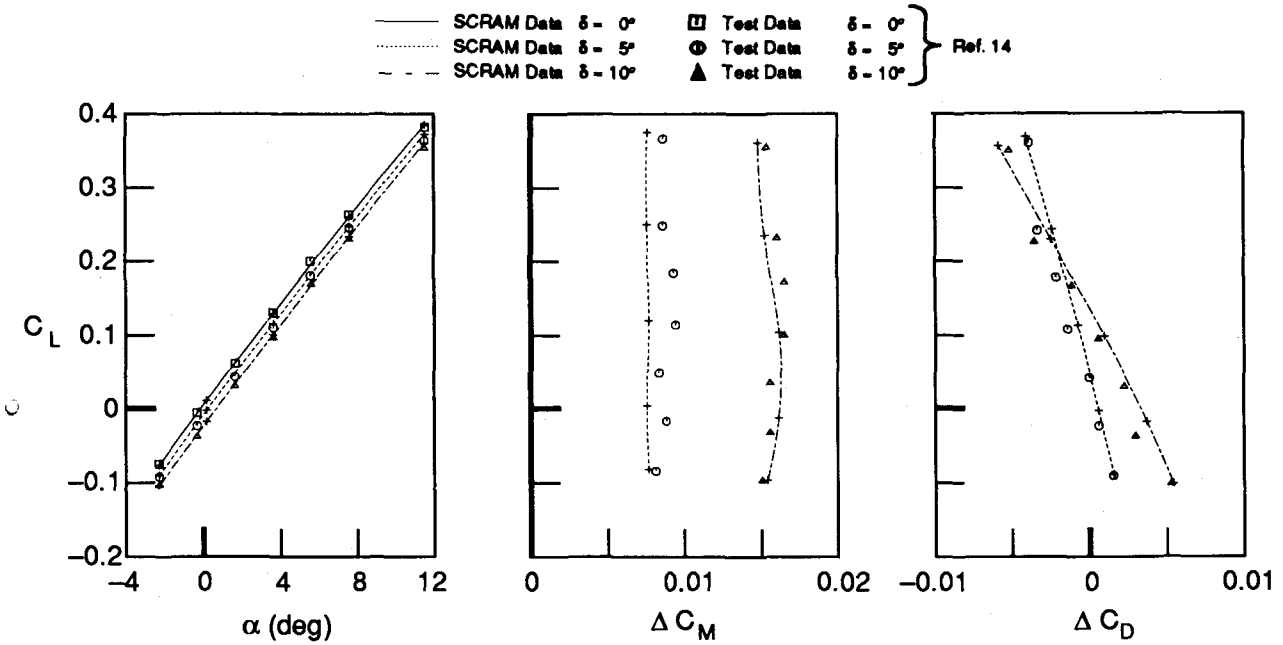

Fig. 16 SSPF Elevon Control Power
$M_\infty = 2.0$

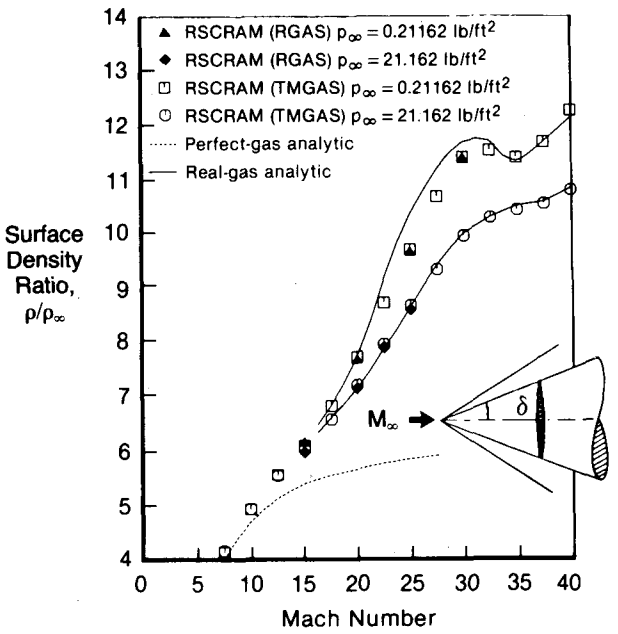

Fig. 17 Surface Density Predictions for a Circular Cone
$\delta = 20°$ $\alpha = 0°$ $T_\infty = 492°$ R

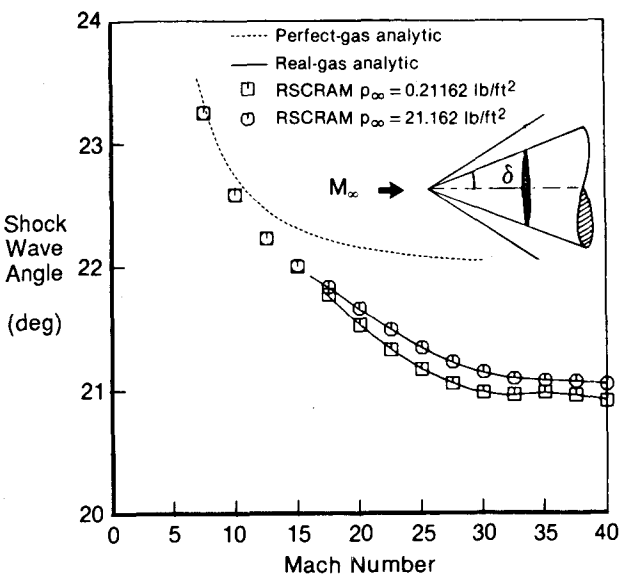

Fig. 18 Shock Wave Angle Prediction for a Circular Cone
$\delta = 20°$ $\alpha = 0°$ $T_\infty = 492°$ R

Summary

Numerical solutions of the Euler equations for supersonic flowfields about various aircraft configurations have been obtained using the SCRAM code. SCRAM is based on the QAZ1D form of the Euler equations and has been shown to be an accurate and efficient prediction method for supersonic/hypersonic inviscid flow about complex configurations. The code has been coupled with a versatile grid generation procedure for construction of high quality computational grids about such shapes. Pressure distributions, forces, and moments compare well with test data for configurations having arbitrary nose shapes, aft-swept wing trailing edges, vertical tails, and control surface deflections. Efficient real gas capability has been validated against analytic cone solutions.

References

1. Verhoff, A., and O'Neil, P. J., "A Natural Formulation for Numerical Solution of the Euler Equations," AIAA Paper No. 84-0163, January 1984.
2. Verhoff, A., and O'Neil, P. J., "Accurate, Efficient Prediction Method for Supersonic/Hypersonic Inviscid Flow," AIAA Paper No. 87-1165, June 1987.
3. Verhoff, A., Stookesberry, D. C., Hopping, B. M., and Michal, T. R., "Supersonic/Hypersonic Euler Flowfield Prediction Method for Aircraft Configurations," *Proc. of the Fourth Symposium on Numerical & Physical Aspects of Aerodynamic Flows*, Long Beach, California, January 16-19, 1989.
4. Agrawal, S., Vermeland, R. E., Verhoff, A., and Lowrie, R. B., "Euler Transonic Solutions over Finite Wings," AIAA Paper No. 88-0009, January 1988.
5. Thompson, J. F., Thames, F. C., and Mastin, C. W., "Automatic Numerical Generation of Body-Fitted Curvilinear Coordinate System for Field Containing Any Number of Arbitrary Two-Dimensional Bodies," *J. Comp. Physics*, Vol. 15, No. 3, July 1974, pp. 299-319.
6. Sorenson, R. L., "A Computer Program To Generate Two-Dimensional Grids About Airfoils and Other Shapes by the Use of Poisson's Equation," NASA TM-81198, May 1980.
7. Pittman, J. L., and Bonhaus, D. L., "A Strake Design Method for Supersonic Speeds and Low Lift," AIAA Paper No. 87-2638, August 1987.
8. Hart, N. E., Dickson, C. R., Boyer, K. V., and Pieper, E. M., "Wind Tunnel Tests on a Hypersonic Research Model in the McDonnell Polysonic Wind Tunnel, Series I," MCAIR Report No. 9981, December 1963.
9. Krieger, R. J., "A Technique for Developing Low Drag Nose Shapes for Advanced Supersonic Missile Concepts," AIAA Paper No. 80-0361, January 1980.
10. McConnell, D. G., "Free-Flight Observation of a Separated Turbulent Flow Including Heat Transfer Up to Mach 8.5," NASA TN D-278, October 1961.
11. Baer, A. L., "Pressure Distributions on a Hemisphere Cylinder at Supersonic and Hypersonic Mach Numbers," AEDC TN-61-96, 1961.
12. Rakich, J.V., "Aerodynamic Performance and Static-Stability Characteristics of a Blunt-Nosed, Boattailed, 13° Half-Cone at Mach Numbers from 0.60 to 5.0," NASA TM X-570, July 1961.

13. Holdaway, G. H., and Mellenthin, J. A., "Investigation at Mach Numbers of 0.20 to 3.50 of Blended Wing-Body Combinations of Sonic Design with Diamond, Delta, and Arrow Plan Forms," NASA TM X-372, August 1960.
14. "Aerodynamic Characteristics of Four Supersonic Cruise Configurations from Mach 1.6 through Mach 2.16," NASA LaRC Unitary Plan Wind Tunnel Test No. 1424, September 1982.
15. Eaton, R. R., and Larson, D. E., "Improved Real Gas Routines for Sandia's NASA AMES Flowfield Program," SAND75-0493, February 1976.
16. Srinivasan, S., Tannehill, J. C., and Weilmuenster, K. J., "Simplified Curve Fits for the Thermodynamic Properties of Equilibrium Air," ERI Project 1626, ISU-ERI-Ames-86401, June 1986.
17. Romig, M. F., "Conical Flow Parameters for Air in Dissociation Equilibrium: Final Results," Convair Scientific Research Laboratory, Research Note No. 14, 1958.